Riblet-induced Pulsating Flow Effect for Drag Reduction in Wall-Bounded Turbulence

Zhaoyang Ou, Wenyuan Zhou, Yalin Tang, Fanhong Liu, Yang He, Weizheng Yuan

Ministry of Education Key Laboratory of Micro/Nano Systems for Aerospace, Key Laboratory of Micro- and Nano-Electro-Mechanical Systems of Shaanxi Province, School of Mechanical Engineering, Northwestern Polytechnical University, 127 Youyi West Road, Xi'an, 710072 China
heyang@nwpu.edu.cn, yuanwz@nwpu.edu.cn

ABSTRACT
Inspired by pulsatile flow in biological systems, this study proposes a novel class of pulsating riblets (PR) featuring non-uniform streamwise spacing. Direct numerical simulations (DNS) and wind tunnel experiments confirm that this design series achieves superior drag reduction compared to conventional shark-skin-inspired riblets. Specifically, the APR500 configuration yields a maximum velocity offset of $\Delta U^+ = 1.26$, corresponding to a peak drag reduction of approximately 12.6% in experimental measurements. Relative to shark-inspired riblet surface, the PR surfaces significantly attenuate Reynolds stresses and successfully induce a pulsatile effect in the near-wall flow, fulfilling the initial mechanistic objectives. The turbulence control exhibited by the PR series provides a promising framework for the future design of high performance drag-reduction microstructures.

INTRODUCITON
Pulsatile flow commonly occurs in fluid transport within biological systems such as blood vessels and trachea at low Reynolds numbers. To reduce fluid shear-induced damage to vascular endothelial cells, rhythmic contractions of the heart or trachea led to intermittent changes in fluid velocity. This pulsatile effect results in lower wall shear stress and higher flow efficiency, thereby enhancing the efficiency of nutrient exchange within organisms (Scarselli et al., 2023; Khan et al., 2025; Dessalles et al., 2021).

The primary mechanism behind this phenomenon is that when turbulent flow is accelerated, it typically leads to a delayed response of the turbulent structures, resulting in a reduction in wall shear stress compared to the quasi-steady value (He et al., 2011). During acceleration, the turbulent structures remain in a frozen state. At this stage, the wall shear stress is dominated by inertia; the acceleration increases the velocity gradient, initially causing the wall shear stress to exceed the quasi-steady value. Shortly afterward, the effect of inertia diminishes, but the frozen turbulent structures require a certain relaxation time to dissipate and reorganize into new structures near the wall. This leads to insufficient momentum transport from the turbulence to the wall, thereby reducing the wall shear stress (Scarselli et al., 2023; Foggi Rota et al., 2025). Even in classical interactions between turbulence flow and the wall, similar behaviour occurs. Although the resulting pulsating flow effect exhibits certain statistical regularity, it lacks controllability through artificial intervention.

In this work, a riblet surface texture designed to induce a pulsating effect and drag reduction in near-wall flow is investigated through numerical simulations and wind experiment. The study examines how variations in the streamwise spacing of riblets generate a pulsating effect of streamwise vortices within the boundary layer. The influence of the pulsating riblets on the velocity distribution in turbulent boundary layers and the resulting pulsating effects are analysed. The impact of this pulsation on wall shear stress is also discussed, with validation provided through wind tunnel experiments.

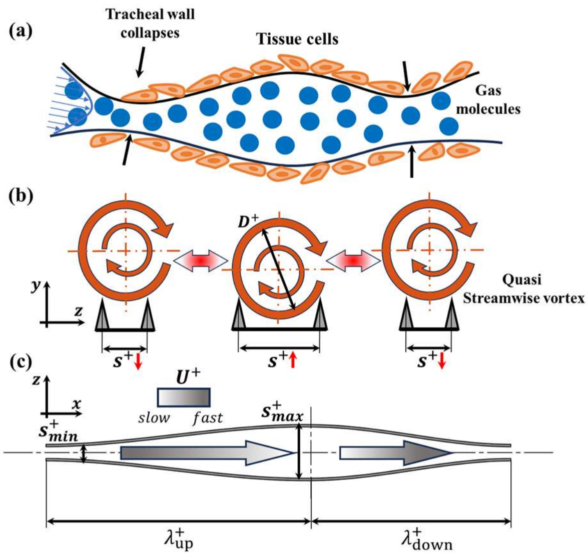

Figure 1. (a) Micro-trachea in the insect respiratory system. (b) Schematic of the control mechanism of streamwise vortices in a turbulent boundary layer through riblet spacing. (c) Configuration of riblet surface inspired by the pulsating flow effect.

METHODLOGY
Problem definition
A pulsating flow effect is achieved through riblet surface, whose streamwise topology plays a critical role in inducing

periodic acceleration and deceleration of near-wall flow. Care must be taken to minimize the drag increase caused by the texture itself, so as to avoid attenuation of the pulsating flow effect. Based on the theoretical understanding of riblet-induced turbulence control in the boundary layer, the streamwise spacing s^+ is varied to mimic the form of a bellows-like mechanism similar to those in insect respiratory systems for enhanced gas exchange—as illustrated in Figure 1. This offers an interesting implementation strategy, and Riblets with graded streamwise spacing s^+ remain relatively unexplored.

The mathematical formula defining the variation and its skewness in the streamwise spacing s^+ of the Pulsating Riblet (PR) is given as follows:

$$s(x) = s^+_{avg} + \Delta s^+ \cos\left(\frac{2\pi x}{\lambda^+}\right) + A\cos\left(\frac{4\pi x}{\lambda^+} + \phi\right)$$

Here, s^+_{avg} denotes the average riblet spacing; $\Delta s^+ = s^+_{max} - s^+_{min}$; while A and ϕ control the degree of skewness ($\lambda^+_{up}/\lambda^+_{down}$) and its direction, with $\phi = \lambda^+_{up}/\lambda^+_{down}$.

Table 1. Pulsating Riblet parameter.

CASE	λ^+_{up}	λ^+_{down}	h^+	a^+	s^+_{avg}
APR500	180	180			
SPR500	180	180			
APR618	137.5/222.5				
SPR618-	137.5	222.5	9	10.5	19.5
SPR618+	222.5	137.5			
APR700	108/252				
SPR700-	108	252			
SPR700+	252	108			

The structural parameters of the pulsating configuration investigated in this study are summarized in Table 1. where 500, 618, and 700 denote the upstream and downstream wavelength ratios $\phi = 0.5, 0.618, 0.7$ of the pulsating riblets, respectively. In addition, we further examine the influence of staggered (SPR and direction by +/-) and aligned (APR) arrangements of pulsating riblets on wall-bounded turbulence, as illustrated in Figure 2 (b) and 2(c).

Numerical procedure

Direct numerical simulation (DNS) was employed for computational analysis. The size of the computational domain is at least $L_x \times L_y \times L_z = 6\delta \times \delta \times 3\delta$, and the streamwise length is adjusted according to the computed friction Reynolds number $Re_\tau = 200$. The domain size satisfies the minimum requirements for DNS (MacDonald et al., 2023). The final dimensions of the computational domain are further adapted to account for the distribution of the riblets. The mesh was constructed using hexahedral structured grids throughout, and all simulation parameters satisfy the resolution requirements for DNS. To compare the flow characteristics over the Pulsating Riblet surface, additional simulations were performed for both a smooth surface and a conventional straight-riblet surface, as shown in Figure 2(a).

Furthermore, flow simulations were conducted over the entire textured surface of the Pulsating Riblet, including configurations with and without skewness, illustrated in Figure 2 (b) and (c), respectively.

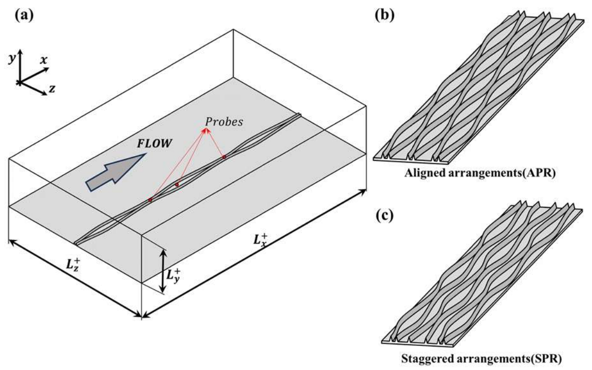

Figure 2. (a) Schematic of the computational domain for flow simulation over the micro-structured surface. (b) Pulsating Riblet surface with aligned arrangements. (c) Pulsating Riblet textured surface with staggered arrangements.

Wind tunnel experiment

The experimental investigations were conducted using the low-speed wind tunnel at Northwestern Polytechnical University, as illustrated in Figure 3(a). It is driven by two servo motors located on either side of the power section, with a total input power of 15 kW and offers a wind speed range of 0~40 m s−1. The turbulence intensity in the test section is less than 1%. Dynamic pressure stability in the central 75% of the test section is better than 0.2%. To ensure fully developed turbulence, a roughness strip was mounted at the leading edge (1100 mm upstream of the sample) to trip the boundary layer. The shear force acting on the sample was measured using an in-house high-precision air-bearing balance (Zhou et al., 2023), with a measurement accuracy of 2.5×10^{-7} N. The test samples were fabricated via two-photon polymerization micro-nano 3D printing (Prismlab China Ltd. MCP-36-3S), which offers a printing resolution of 2 μm and the area of 30 mm × 60 mm, as shown in Figure 3(a) and (b). The non-dimensional parameters of the structural samples are consistent with those used in the simulations, and the physical dimensions were determined based on the local flow conditions in the wind tunnel.

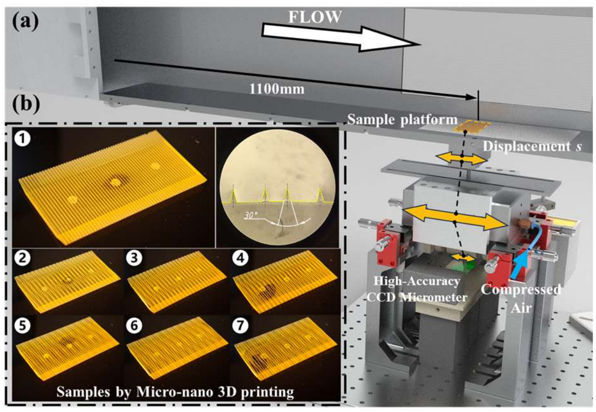

Figure 3. (a) Low-speed wind tunnel and in-house high-precision air-bearing balance at Northwestern Polytechnical University. (c) Structural sample fabricated via micro-nano 3D printing.

The experiments were conducted under controlled ambient conditions, with the temperature fluctuations strictly maintained within $25℃ + 2℃$ to ensure the stability of fluid properties. To validate the experimental facility, initial benchmarks were performed using a smooth reference sample. As illustrated in Figure 4, the measured skin-friction coefficients C_f exhibit excellent agreement with Schlichting's empirical correlation (Schlichting et al., 2016), thereby confirming the operational stability and reliability of the wind tunnel system. For each PR, ten independent trials were executed at a freestream velocity of $U_\infty = 5m/s$. The measurement uncertainty of the drag coefficient was consistently constrained within 3%, ensuring high repeatability across all tested cases.

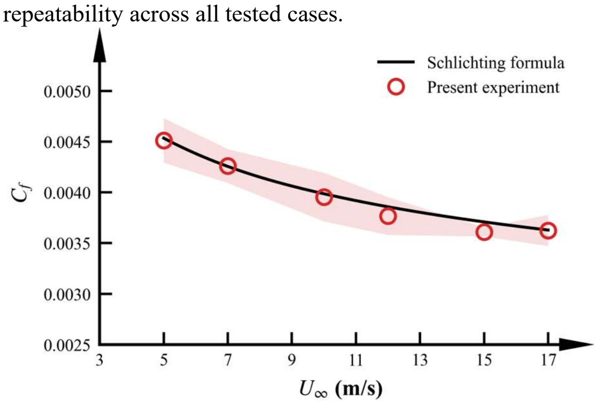

Figure 4 Comparison of measured skin-friction coefficients $\boldsymbol{C_f}$ with Schlichting's empirical correlation.

RESULTS

Drag reduction

The ensemble averaged velocity shift, $\Delta U^+ = \bar{U}_{smoot} - \bar{U}_{PR}$, is derived from the statistical averaging of DNS flow field data across various structural configurations, as illustrated in Figure 5. An upward displacement of the ensemble averaged streamwise velocity profile signifies a reduction in skin friction. The drag reduction *DR* can be quantified through the Hama roughness function evaluated at $z = \delta$, expressed as:

$$DR = \frac{\Delta C_f}{C_f} = \left(1 - \frac{\Delta U^+}{U_\delta^+}\right)^{-2} - 1 \sim 2\Delta U^+/U_\delta^+$$

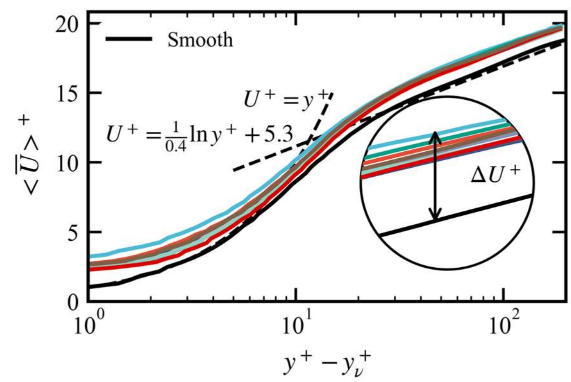

Figure 5 Ensemble averaged Streamwise Velocity $<\bar{\boldsymbol{U}}>^+$

The final drag reduction (*DR*) measured from the wind tunnel experiments are presented in Figure 6. The experimental *DR* values exhibit consistency with those obtained from DNS. Specifically, the uniform riblet (UR) configuration achieves a maximum drag reduction of approximately 8.5% in the experiments, with a corresponding ensemble averaged velocity shift of ΔU^+=1.08 at $s^+ \approx 18$ and $Re_\tau \approx 492$. These quantitative findings align well with established experimental and DNS results reported in the literature (Bechert et al., 1997; Modesti et al., 2021; Inasawa et al., 2024).

Regarding the drag reduction *DR* of the pulsating riblet cases, several discernible trends are identified. Notably, the APR500 configuration exhibits superior performance compared to SPR500—an observation that deviates from our initial hypothesis. From a topological perspective, the SPR series, characterized by pairs of counter-oriented riblets on both sides, was expected to induce more intensive flow pulsations. Interestingly, this expected topological advantage is only manifested in the skewed pulsating riblet cases; specifically, SPR618+ and SPR700+ consistently outperform their asymmetric counterparts, APR618 and APR700, in terms of drag-reducing performance.

In general, the drag reduction performance of skewed pulsating riblet configurations is found to be inferior to that of their aligned counterparts. This performance degradation is primarily attributed to the potential escalation of pressure drag over the textured surface induced by the skewness. A clear trend is observed wherein an increase in skewness correlates with a systematic deterioration of drag-reducing efficiency. Notably, the aligned pulsating riblets appear to be relatively insensitive to skewness. This is attributed to the fact that the aligned configuration inherently induces a topologically staggered arrangement of skewness orientations within each pulsation cycle.

Intriguingly, while pulsating riblets inevitably incur additional pressure drag due to the streamwise variations in their cross-section, the resulting pulsating effect appears to largely offset this penalty. Consequently, the drag reduction *DR* performance of the pulsating configurations remains comparable to that of the UR, with even the least effective case (APR618) maintaining a *DR* of $\Delta U^+ = 0.89$. This observation underscores that the pulsating effect introduces a distinct modulation to the underlying drag reduction mechanism, potentially offering a unique pathway for turbulence control that differs from conventional riblet theories.

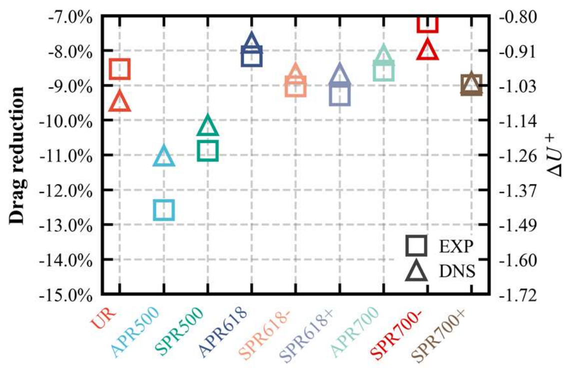

Figure 6 Experimental and DNS drag reduction results for all samples.

The surface topology of the APR500 specimen closely resembles the configuration investigated by Sasamori et al. (Sasamori et al., 2014), with the primary distinction residing in the cross-sectional geometry (see Figure 7). Specifically, the present study employs a triangular cross-section with a 30° angle. For Uniform Riblets, a 30° triangular cross-sectional profile has been shown to yield superior drag-reduction performance (Endrikat et al., 2021), a finding that is further corroborated by our present experimental observations.

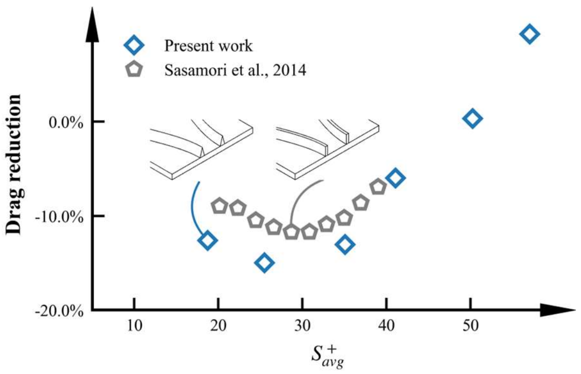

Figure 7 Drag reduction performance of APR500 for $S^+_{avg} = 18\sim57$ and comparison with experimental data from Sasamori. (Sasamori et al., 2014).

Turbulence statistics

The ensemble-averaged streamwise velocity and Reynolds stress profiles for all cases are presented in Figure 5 and Figure 8 respectively. For all configurations, the profiles have been adjusted according to their virtual origins y^+_v, the determination of which follows the methodology established by Endrikat et al. (Endrikat et al., 2021).

Consistent with the preceding comparative analysis of drag reduction performance, the APR500 configuration yields the minimum ΔU^+, signifying the most effective drag reduction among all cases. Nevertheless, several distinct features observed in the ensemble-averaged Reynolds stress profiles have emerged, warranting further investigation into the underlying turbulence modulation.

The present numerical investigation employs direct numerical simulation (DNS) of a periodic channel flow driven by a constant pressure gradient. Under this framework, the behaviour of the ensemble-averaged Reynolds stresses—specifically the streamwise normal stress ($<\overline{u'u'}>^+$) and the shear stress ($<\overline{u'v'}>^+$)—deviates from typical experimental observations. In conventional experiments, drag-reducing riblets typically suppress Reynolds stresses relative to the smooth-wall baseline. In contrast, DNS results reveal that for riblets of the same geometry, an increase in drag-reduction efficiency is associated with a less pronounced reduction in Reynolds stress magnitudes. However, when comparing across distinct various riblet types, superior drag-reduction performance consistently correlates with a systematic lowering of both stress components.

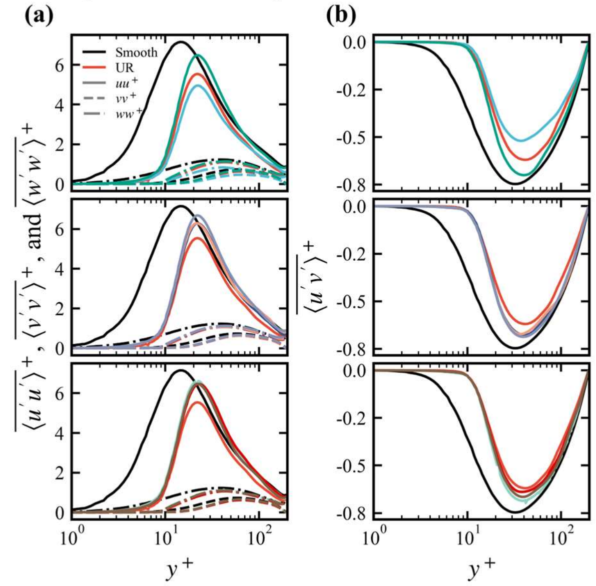

Figure 8 Profiles of ensemble averaged Reynolds stresses: (a) streamwise ($\boldsymbol{u'^+}$), spanwise ($\boldsymbol{v'^+}$), wall-normal ($\boldsymbol{w'^+}$) velocity, and (b) Reynolds shear stresses ($\overline{<\boldsymbol{u'v'}>^+}$)

An analysis of the turbulence statistics for the APR500 and SPR500 configurations, relative to the smooth-wall and UR

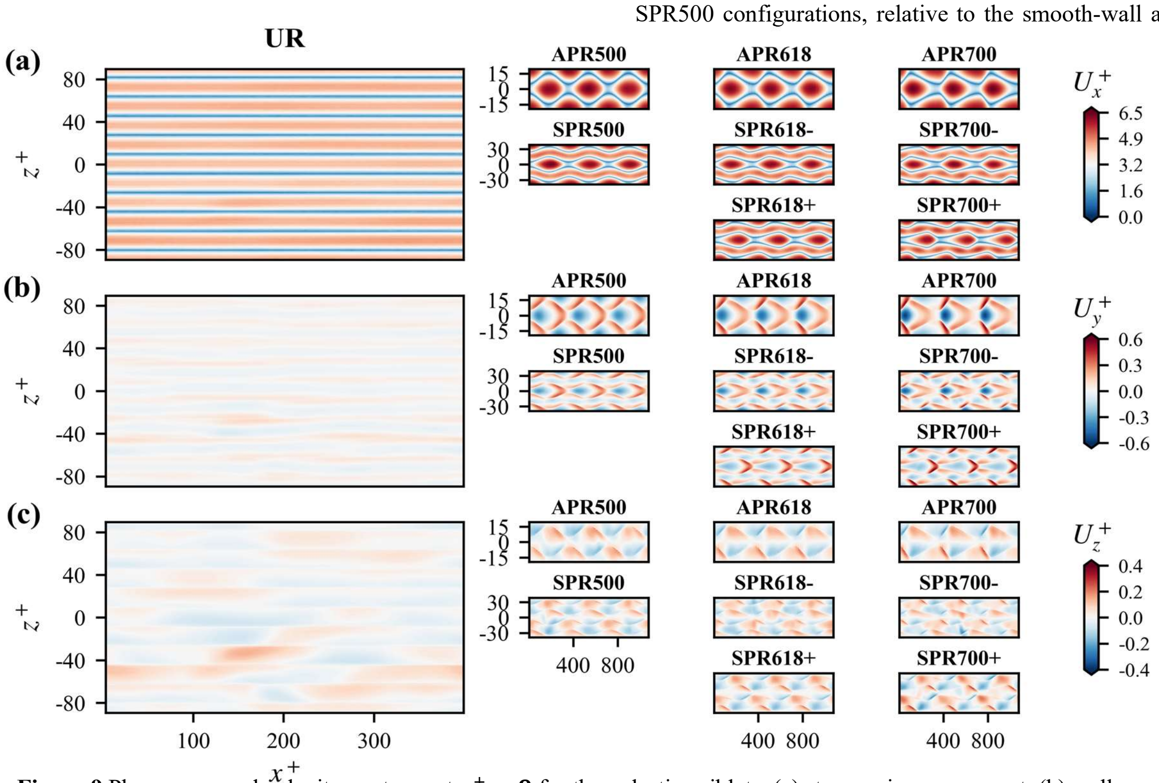

Figure 9 Phase-averaged velocity contours at $\boldsymbol{y^+ = 9}$ for the pulsating riblets: (a) streamwise component; (b) wall-normal component; (c) spanwise component.

baselines, reveals that APR500 yields the most pronounced suppression of both streamwise normal and shear stresses. Notably, while the drag-reduction performance of SPR500 lies between those of the UR and APR500 cases, it exhibits the least reduction in Reynolds stress magnitudes; this suggests a distinctive modulation of near-wall turbulence induced by the SPR topology. This unique behaviour is further corroborated by the 618-series (APR618, SPR618−, and SPR618+), where SPR618+ demonstrates the minimal reduction in Reynolds stresses. Although SPR618− and APR618 exhibit comparable levels of stress suppression, the DR efficiency of both SPR variants is nearly identical and superior to that of APR618, further underscoring the atypical mechanisms introduced by the SPR topological arrangement. In contrast, the 700-series follows a more conventional logic: SPR700+ achieves superior performance with slightly greater stress reduction than APR700. However, despite the substantial Reynolds stress suppression observed in the SPR700− case, its overall DR remains limited, which is likely attributable to a compensatory increase in pressure drag. Collectively, these findings indicate that the topological layout and the associated upstream/downstream skewness of the SPR/APR configurations introduce a complex interplay of drag-reduction and drag-enhancement mechanisms.

Skin friction is primarily attributed to the transport of turbulent kinetic energy (TKE) mediated by turbulent eddies (Pope, 2001).

$$\frac{\partial k}{\partial t} + \bar{u} \cdot \nabla k = P - \epsilon + T_{nl} + T_p + T_\nu$$

Where k denotes the turbulent kinetic energy (TKE), P and ϵ signify the production and dissipation rates, respectively; T_ν is the molecular viscous diffusion term, while T_{nl} and T_p represent the transport terms of TKE.

It follows from the TKE budget that in channel flows, the terms T_{nl} and T_p primarily fulfill a redistributive function; however, by altering the spatial allocation of energy, they fundamentally modulate the resulting shear stress distribution. Consequently, the analysis of Reynolds stress profiles suggests that the APR/SPR configurations and their associated skewness exert a significant influence on these transport terms, thereby either enhancing or impairing the overall drag-reduction performance.

Riblet pulsating effects

As demonstrated in Figure 9(a), all pulsating riblet configurations validate the initial hypothesis. Relative to the UR case, these Pulsating Riblet cases exhibit a distinct pumping effect in the mean streamwise velocity, which is further characterized by a discernible spatial (or phase) offset of the velocity peaks. Furthermore, it is observed that the SPR configuration does not significantly augment the mean streamwise velocity within the current x-z plane, although such effects may potentially manifest at higher wall-normal elevations. Within the outer grooves of the SPR topology, the mean streamwise velocity remains comparable to that of the UR case, suggesting that the inertial motions of the boundary layer have yet to penetrate these recessed regions. Notably, the velocity contours for the SPR618+/- and SPR700+/- cases reveal distinct non-uniformities in the flow over the peripheral riblets. This observation further underscores that the topological skewness induces an asymmetric streamwise pumping effect, thereby leading to a non-reciprocal modulation of the near-wall momentum.

Building upon these observations, Figure 9(b) and (c) illustrate that the spanwise variations in pulsating riblet spacing induce pronounced and systematic oscillations in the velocity components (U_y^+ and U_z^+). This phenomenon signifies a spatial redistribution of the momentum field, which partially attenuates the overall drag reduction performance. Specifically, regions exhibiting extreme wall-normal velocity U_y^+ values—whether maxima or minima—indicate localized and intense flow impingement. Such impingement inevitably incurs a significant pressure drag penalty, as evidenced by the monotonic decrease in efficiency across the series: DR(APR500) > DR(APR618) > DR(APR700). Notably, Figure 9 (b) reveals that the SPR+ series exhibits larger peak magnitudes and lower minima in U_y^+ compared to both the APR and SPR- configurations. While the SPR+ variants generally outperform their APR and SPR- counterparts of the same skewness, this trend is conspicuously absent in the 500 series. This discrepancy suggests the involvement of additional competing mechanisms, the detailed exploration of which is reserved for future discussion.

Furthermore, profiles of the mean streamwise velocity along the pulsating riblet centerline were extracted at various wall-normal locations to elucidate the spatial evolution of the pulsating effect across all cases, as shown in Figure 10. It is observed that the APR500 and SPR500 configurations exhibit nearly identical flow control efficacy, with the most pronounced modulation in the mean streamwise velocity—reaching an amplitude of approximately 5m/s—occurring at $y^+ = 9$. This modulation is inherently accompanied by a discernible skewness in the velocity pulsation. As y^+ increases, the riblet-induced pulsating effect undergoes systematic attenuation; by $y^+ = 20$, as the flow approaches the inception of the outer layer ($y^+ > 30$), the pulsating effect virtually diminishes and becomes negligible.

Similarly, across the APR, SPR-, and SPR+ cases, the skewness of the mean streamwise velocity profiles becomes increasingly pronounced. According to the drag-reduction mechanisms identified in pulsating pipe flows (Scarselli et al., 2023), the relative durations of the acceleration and quiescent phases are critical for energy efficiency. Although the SPR-series achieves a shortened acceleration distance, the resulting

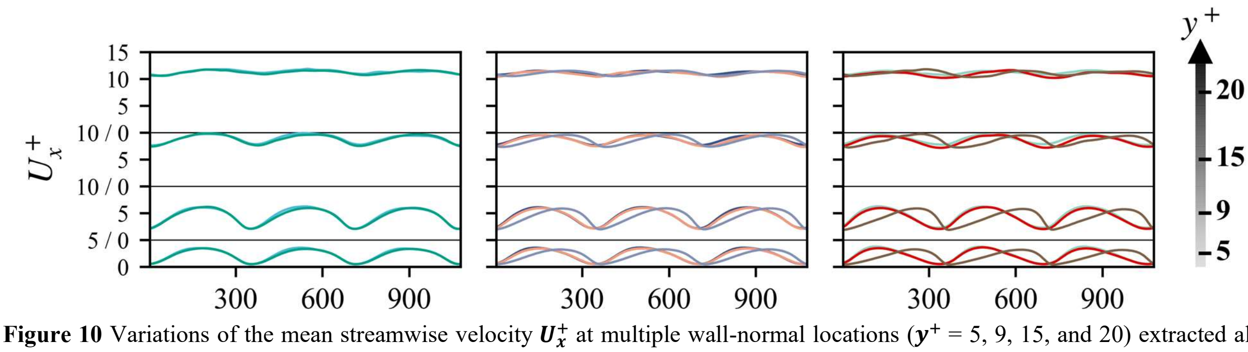

Figure 10 Variations of the mean streamwise velocity U_x^+ at multiple wall-normal locations (y^+ = 5, 9, 15, and 20) extracted along the riblet spacing centerline: (left) APR500 and SPR500 cases; (middle) APR618, SPR618−, and SPR618+ cases; (right) APR700, SPR700−, and SPR700+ cases.

drag reduction performance in both experimental and DNS data remains suboptimal, potentially due to the absence of a distinct quiescent phase. Notably, this intense skewness of the pulsating effect persists up to $y^+ = 20$. While it has yet to trigger pulsations within the turbulent structures of the logarithmic region—the primary locus of Reynolds stress production—it demonstrates the capacity to extend the pulsating influence to higher wall-normal elevations. This extension of the pulsating effect remains a focal point for our future investigations.

Finally, the mean viscous–inertial interface—alternatively characterized as the envelope of coherent structures within the boundary layer—is extracted for the APR and SPR configurations, as depicted in Figure 11. Following a threshold criterion of 0.01 k^+_{max}, it is conventionally understood that for drag-reducing riblets—particularly those operating within the viscous regime—a smoother interface is conducive to performance, as it shields the viscous sublayer from turbulent incursions by guiding the instantaneous velocity vectors. Contrary to this convention, the present APR and SPR topologies do not shield the viscous sublayer; instead, they induce a systematic corrugation of the viscous interface. Furthermore, both configurations accentuate the streamwise vorticity ω_x , which, according to the established self-sustaining mechanism of near-wall coherent structures (Schoppa & Hussain 2002), would typically strengthen the vortex regeneration cycle and lead to a drag penalty. However, our results demonstrate otherwise. This discrepancy is likely attributable to the profound modifications in the streamwise velocity gradients; specifically, the spanwise gradient $\partial u/\partial x$ appears to be the dominant governing factor on pulsating surfaces, as clearly evidenced in Figure 11, which underscores the primary design objective of the pulsating riblet concept.

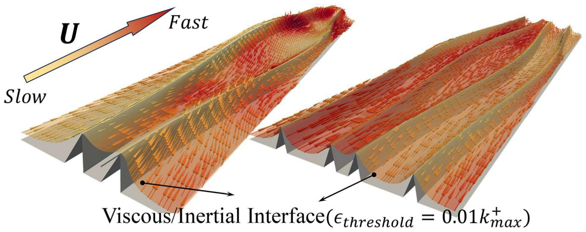

Figure 11 Instantaneous velocity contours and the viscous–inertial interface over the (left) APR500 and (right) SPR500 surfaces.

CONCLUDING REMARKS

This study introduces streamwise spacing variations in riblets to achieve pulsating control of velocity components in wall-bounded turbulence. The drag-reduction performance of aligned (APRs), staggered (SPRs), and skewed pulsating configurations was systematically evaluated and validated. Results demonstrate that the proposed APR500 configuration exhibits superior performance at $Re_\tau = 200$ and a free-stream velocity of 5m/s, yielding $\Delta U^+ = 1.26$ and DR=12.6%. This performance is accompanied by a significant attenuation of Reynolds stresses and a pronounced pulsating effect on the near-wall turbulent flow, fulfilling the initial design objectives. While preliminary conclusions have been reached, further investigation is required to establish the complete scaling laws for PR performance ($\Delta U^+ - s^+$). Notably, the SPR configuration exhibits distinct control effects not captured by Reynolds stress profiles, while topological skewness incurs a significant pressure drag penalty.

The present study introduces multi-dimensional riblet geometries, each yielding distinct flow control characteristics. Consistent with our previous findings (Ou et al., 2026), geometric variations continue to offer significant potential for further performance optimization.

ACKNOWLEDGEMENT

The authors gratefully acknowledge the support of National Key Research and Development Program of China (2024YFB3408800) and Innovation Foundation for Doctor Dissertation of Northwestern Polytechnical University (ZX2025014). We also acknowledge the HPC Service provided by the Computing Center in Xi'an and the technology service supported by SiroMEMS Co., Ltd.

SAMPLE REFERENCES

Scarselli, D., Lopez, J. M., Varshney, A., & Hof, B. (2023). Turbulence suppression by cardiac-cycle-inspired driving of pipe flow. *Nature*, 621(7977), 71-74.

Khan, S., & Staples, A. E. (2025). Mechanisms of insect respiration. *Nature Reviews Physics*, 1-14.

Dessalles, C. A., Leclech, C., Castagnino, A., & Barakat, A. I. (2021). Integration of substrate-and flow-derived stresses in endothelial cell mechanobiology. *Communications Biology*, 4(1), 764.

He, S., Ariyaratne, C., & Vardy, A. E. (2011). Wall shear stress in accelerating turbulent pipe flow. *Journal of Fluid Mechanics*, 685, 440-460.

Foggi Rota, G., Monti, A., Rosti, M. E., & Quadrio, M. (2023). Saving energy in turbulent flows with unsteady pumping. *Scientific Reports*, 13(1), 1299.

MacDonald, M., Chung, D., Hutchins, N., Chan, L., Ooi, A., & García-Mayoral, R. (2017). The minimal-span channel for rough-wall turbulent flows. *Journal of Fluid Mechanics*, 816, 5-42.

Zhou, W., Liu, X., Sun, Y., Lyu, X., He, Y., & Yuan, W. (2025). Design and validation of an air-bearing-based micro skin-friction balance for small area samples. *Experimental Thermal and Fluid Science*, 164, 111433.

Schlichting, H., & Gersten, K. (2016). *Boundary-layer theory*. springer.

Modesti, D., Endrikat, S., Hutchins, N., & Chung, D. (2021). Dispersive stresses in turbulent flow over riblets. *Journal of Fluid Mechanics*, *917*, A55.

Bechert, D. W., Bruse, M., Hage, W. V., Van der Hoeven, J. T., & Hoppe, G. (1997). Experiments on drag-reducing surfaces and their optimization with an adjustable geometry. *Journal of Fluid Mechanics*, 338, 59-87.

Inasawa, A., Taniguchi, R., Asai, M., Sasamori, M., & Kurita, M. (2024). Experimental investigation of yaw-angle effects on drag reduction rate for trapezoidal riblets. *Experiments in Fluids*, *65*(3), 29.

Sasamori, M., Mamori, H., Iwamoto, K., & Murata, A. (2014). Experimental study on drag-reduction effect due to sinusoidal riblets in turbulent channel flow. *Experiments in Fluids*, *55*(10), 1828.

Endrikat, S., Modesti, D., García-Mayoral, R., Hutchins, N., & Chung, D. (2021). Influence of riblet shapes on the occurrence of Kelvin–Helmholtz rollers. *Journal of Fluid Mechanics*, *913*, A37.

Pope, S. B. (2001). Turbulent flows. *Measurement Science and Technology*, *12*(11), 2020-2021.

Schoppa, W., & Hussain, F. (2002). Coherent structure generation in near-wall turbulence. *Journal of fluid Mechanics*, *453*, 57-108.

Ou, Z., Zhou, Z., Zhang, Z., Wang, S., He, Y., & Yuan, W. (2026). Metasurface of fluid mechanics for efficient turbulence drag reduction. *Renewable Energy*, *256*, 124555.